### **OPEN ACCESS**



# Electron Injection via Modified Diffusive Shock Acceleration in High-Mach-number Collisionless Shocks

A. Grassi <sup>1,2</sup>, H. G. Rinderknecht <sup>3</sup>, G. F. Swadling <sup>4</sup>, D. P. Higginson <sup>4</sup>, H.-S. Park <sup>4</sup>, A. Spitkovsky <sup>5</sup>, and F. Fiuza <sup>6,2</sup>, LULI, CNRS, CEA, Sorbonne Université, École Polytechnique, Institut Polytechnique de Paris, F-75255 Paris, France; anna.grassi@polytechnique.edu <sup>2</sup> High Energy Density Science Division, SLAC National Accelerator Laboratory, Menlo Park, CA 94025, USA; frederico.fiuza@tecnico.ulisboa.pt <sup>3</sup> Laboratory for Laser Energetics, University of Rochester, Rochester, NY, USA <sup>4</sup> Lawrence Livermore National Laboratory, Livermore, CA, USA <sup>5</sup> Princeton University, Princeton, NJ, USA

<sup>6</sup> GoLP/Instituto de Plasmas e Fusão Nuclear, Instituto Superior Técnico, Universidade de Lisboa, 1049-001 Lisbon, Portugal Received 2023 September 8; revised 2023 November 14; accepted 2023 November 16; published 2023 November 28

### Abstract

The ability of collisionless shocks to efficiently accelerate nonthermal electrons via diffusive shock acceleration (DSA) is thought to require an injection mechanism capable of preaccelerating electrons to high enough energy where they can start crossing the shock front potential. We propose, and show via fully kinetic plasma simulations, that in high-Mach-number shocks electrons can be effectively injected by scattering in kinetic-scale magnetic turbulence produced near the shock transition by the ion Weibel, or current filamentation, instability. We describe this process as a modified DSA mechanism where initially thermal electrons experience the flow velocity gradient in the shock transition and are accelerated via a first-order Fermi process as they scatter back and forth. The electron energization rate, diffusion coefficient, and acceleration time obtained in the model are consistent with particle-in-cell simulations and with the results of recent laboratory experiments where nonthermal electron acceleration was observed. This injection model represents a natural extension of DSA and could account for electron injection in high-Mach-number astrophysical shocks, such as those associated with young supernova remnants and accretion shocks in galaxy clusters.

Unified Astronomy Thesaurus concepts: Cosmic ray sources (328); Supernova remnants (1667); Laboratory astrophysics (2004)

### 1. Introduction

Astrophysical observations have long shown the ability of high-Mach-number collisionless shocks to accelerate nonthermal electrons, from supernovae remnants (SNRs) to accretion shocks in galaxy clusters (Völk et al. 2005; Molnar et al. 2009; Ha et al. 2023). These shocks are mediated by plasma instabilities, which produce and amplify magnetic fields and dissipate the flow energy by heating the plasma and accelerating particles. The dominant particle acceleration mechanism thought to operate at astrophysical shock waves is diffusive shock acceleration (DSA; Axford et al. 1977; Krymskii 1977; Bell 1978a, 1978b; Blandford & Ostriker 1978), which corresponds to a first-order Fermi process. Particles gain energy by repeatedly crossing the shock front while scattering off converging magnetic field turbulence on both sides of the shock. DSA is well understood in the testparticle limit and, for strong shocks, produces power-law energy spectra with a universal slope  $\varepsilon^{-2}$  (with  $\varepsilon$  the particle energy; Drury 1983; Blandford & Eichler 1987) that can be consistent with the spectrum of galactic cosmic rays  $\varepsilon^{-2.7}$  when nonlinear corrections (Blandford & Eichler 1987; Diesing & Caprioli 2021) and diffusion in the galactic medium is taken into account (Blasi & Amato 2012). However, in order for particles to cross the shock front they must undergo preacceleration, causing their gyroradii to reach a size comparable to or greater than the shock transition size, which

Original content from this work may be used under the terms of the Creative Commons Attribution 4.0 licence. Any further distribution of this work must maintain attribution to the author(s) and the title of the work, journal citation and DOI.

is typically dictated by the gyroradius of the inflowing ions. This is known as the "injection problem" and it poses a significant challenge, particularly for electrons due to their relatively small mass (Treumann 2009).

Two main injection mechanisms are often invoked: shock drift acceleration (SDA; Hudson & Kahn 1965; Begelman & Kirk 1990) and shock surfing acceleration (SSA; Sagdeev 1966; Katsouleas & Dawson 1983). In SDA, particles gyrating in the ambient magnetic field gain energy as their guiding center moves along the convective electric field due to drifts associated with the magnetic field gradient at the shock. Conservation of magnetic moment limits the energy gain during the interaction of the particles with the shock. In SSA, particles reflected by the shock potential can be trapped between the shock front and the upstream, and gain energy by the convective electric field.

Spacecraft observations have been shaping our understanding of planetary shocks, suggesting that both electrons and ions can be efficiently accelerated via SDA in the region where the shock is quasi-perpendicular (Sarris & Krimigis 1985; Johlander et al. 2021). However, observations of planetary shocks are typically limited to low/moderate Mach numbers ( $M \lesssim 10$ ); electron injection in very high-Mach-number shocks ( $M \gtrsim 100$ ) remains an important challenge that is critical to understanding particle acceleration in SNR and galaxy cluster accretion shocks.

In the last decades, kinetic simulations have been playing an important role in the characterization of particle acceleration at shocks by providing a self-consistent description of the shock dynamics. Most numerical studies of high-Mach-number shocks have focused on quasi-perpendicular configurations

and indicate that electrons can gain energy by a combination of different effects, including scattering off Whistler waves (Levinson 1992), SSA in electrostatic modes driven by the Buneman instability (Hoshino & Shimada 2002; Matsumoto et al. 2012), a combination of SDA and SSA (Amano & Hoshino 2007, 2008), and magnetic reconnection (Matsumoto et al. 2015; Bohdan et al. 2020). In addition, microturbulence produced at the shock has been suggested to help electron injection directly via second-order Fermi acceleration (Bohdan et al. 2017; Ha et al. 2023) or by increasing the efficiency of SDA due to the increased time over which particles remain confined close to the shock front, in a process termed stochastic SDA (SSDA; Matsumoto et al. 2017; Katou & Amano 2019; Amano et al. 2020). There is still no consensus on whether these mechanisms can effectively operate in high-Machnumber astrophysical shocks and how they control electron injection.

Laboratory experiments are opening new, complementary paths to investigate the microphysics governing astrophysical shocks at kinetic scales, which are not accessible by observations. While the scales associated with laboratory experiments are vastly different from those of astrophysical shocks, it is becoming possible to drive energetic plasmas where the dimensionless parameters that control the microphysical behavior (e.g., Mach number, flow velocity normalized to the speed of light, and collisional mean free path normalized to the system size) match those of astrophysical plasmas enabling formal scaling of the processes between both systems (Ryutov et al. 2012). Recently, experiments at the National Ignition Facility (NIF) have used energetic lasers to drive high-Mach-number plasma flows, demonstrating the formation of collisionless shocks in conditions relevant to young SNRs (Fiuza et al. 2020). In these experiments, shock formation follows from the interpenetration of two counterstreaming flows with velocity  $\gtrsim 1000 \,\mathrm{km \, s^{-1}}$  produced by laser ablation of two solid targets. Measurements of the electron spectra show the acceleration of nonthermal electrons up to 500 keV, which is more than 100 times the measured shocked electron thermal energy  $T_e \simeq 3 \text{ keV}$  (Fiuza et al. 2020). These results offer a unique opportunity to benchmark numerical simulations and help validate models of electron injection in shocks.

In this paper, we present the results of kinetic simulations of the NIF experimental conditions that indicate that kinetic-scale turbulence produced by the ion Weibel (Weibel 1959), or current filamentation (Fried 1959), instability leads to effective electron injection via a first-order Fermi process occurring within the shock transition. We introduce a description of this process as a modified version of DSA, here termed modified-DSA (m-DSA), in which we account for the flow velocity profile at the shock transition, in contrast to conventional DSA in which the shock front is considered an infinitely sharp transition. This model is consistent with the simulation results and represents a natural mechanism for electron injection in high-Mach-number shocks.

# 2. Simulations of NIF Experiments

The experimental observation of nonthermal electron acceleration to  $>100\times$  their thermal energy at the shock, in a few nanoseconds of the shock evolution, can help benchmark models of electron injection in high-Mach-number shocks. In order to gain further insight into the shock structure and to identify the

electron acceleration mechanism, we perform 2D3V fully kinetic simulations of the experimental conditions with the particle-incell (PIC) code OSIRIS 4.0 (Fonseca et al. 2002, 2008). We consider two nonrelativistic counterpropagating electron-ion plasmas with nonuniform velocity and density profiles matching the NIF laser-produced flows (see Fiuza et al. 2020 and Grassi & Fiuza 2021 for more details). These profiles are in good agreement with hydrodynamic simulations (Marinak et al. 2001). with measurements of the plasma density at the midplane from the NIF experiments, and with the well-established self-similar solution (Gurevich et al. 1966), which predicts a flow velocity that decreases with time as  $\propto t^{-1}$  at the midplane. We consider initially unmagnetized plasmas as appropriate for the experiments and given that we are interested in studying the high Mach number limit. The sonic Mach number is  $M_s \simeq 35$  for the initial velocity of the counterstreaming flows. We model the interaction between the two flows in a box of extension 11,000  $\times$  800 $(c/\omega_{pe})^2$ , where c is the speed of light in vacuum and  $\omega_{pe}=(4\pi n_0 e^2/m_e)^{1/2}$  is the electron plasma frequency,  $n_0$  the maximum density of the overlapped plasmas, and -e and  $m_e$ the electron charge and mass. We used a spatial resolution of  $\simeq 0.4 \, c/\omega_{pe}$  and 50 macro-particles per cell with a third-order particle interpolation scheme for improved numerical accuracy. We have tested the convergence of the numerical results by varying the resolution in the range  $(0.07-0.4)c/\omega_{pe}$ , the number of particles per cell between 25 and 200, and the ion-to-electronmass ratio between 128 and 512, observing overall agreement on the shock structure and nonthermal electron spectrum. The boundary conditions for both particles and fields are open along the flow direction and periodic transversely. To maintain a reasonable computational cost, we employed a reduced ion mass-to-charge ratio  $m_i/(m_e Z) = [128-512]$ , with  $m_i$  the ion mass and Z the ion charge number, and an initial peak flow velocity  $|u(t \simeq 0)| \simeq 0.25c$ , which is  $\simeq 30 \times$  higher than the experimental one. For this scaled-up velocity, the interaction remains nonrelativistic and dominated by electromagnetic instabilities so that the properties of the shock structure and magnetic fields can be formally scaled to the experimental conditions (Ryutov et al. 2012) as also shown by Bohdan et al. (2021).

The main simulation results are shown in Figure 1. As the plasma flows interact, strong B-fields perpendicular to the propagation direction are produced through the Weibel, or current-filamentation, instability (Fried 1959; Weibel 1959; Medvedev & Loeb 1999), with a spatial scale comparable to the ion skin depth,  $c/\omega_{ni}$ , and a few percent of the flow kinetic energy is converted into electromagnetic energy (Spitkovsky 2007; Kato & Takabe 2008; Lemoine et al. 2019; Swadling et al. 2020). During the nonlinear evolution of the instability, the spatial scale of the magnetic field structures increases and becomes turbulent, as shown in Figure 1(a). As the coherent length of the amplified magnetic field becomes comparable to the gyroradius of the incoming flow ions in the local field, the ions are effectively slowed down and compressed. Two collisionless shocks are formed, whose front widths are comparable to the local ion gyroradius and propagate outward with respect to the midplane (as highlighted by the black arrows).

The temporal evolution of the electron energy spectrum in the downstream region clearly shows the development of a nonthermal tail that extends to  $\gtrsim 100 k_{\rm B} T_e$ , where  $T_e$  is the shocked electron temperature computed in a downstream region of extension  $\simeq 200 \ c/\omega_{pi}$  around the center of interaction

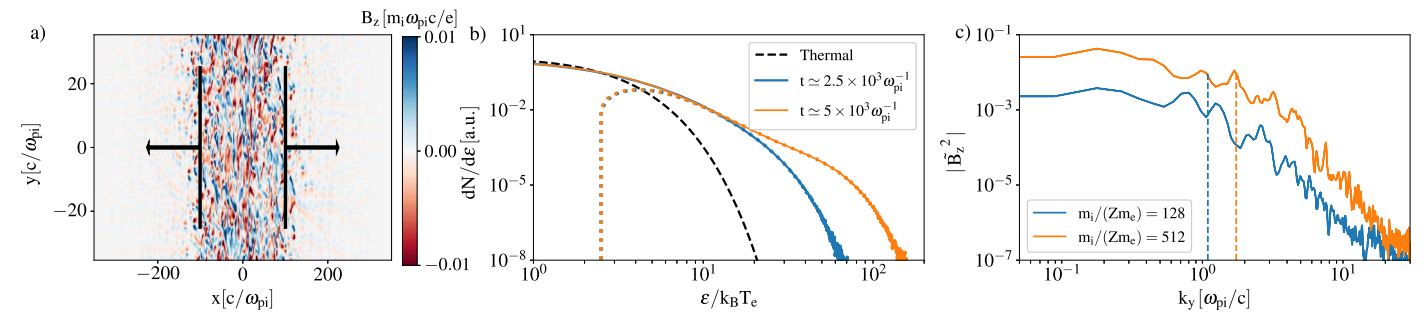


Figure 1. (a) Magnetic field  $B_z$  at  $t_{sel} \simeq 2.5 \times 10^3 \, \omega_{pl}^{-1}$ . The shock front positions and their propagation direction are highlighted by the black lines and arrows. (b) Energy spectrum of the electrons in a downstream region extending for  $\simeq \pm 100 \, c/\omega_{pi}$  at  $t_{sel} \simeq 2.5 \times 10^3 \, \omega_{pl}^{-1}$  (blue plain line) and  $t = 5 \times 10^3 \, \omega_{pl}^{-1}$  (orange plain line). The thermal component given by the Maxwellian fit (black dashed line) and the nonthermal components (obtained by subtracting the thermal component from the full distribution) are shown at both times (blue and orange dotted lines, respectively). (c) Magnetic power spectrum in the shock downstream  $-22 < x \, \omega_{pi}/c < 22$  at  $t \simeq 1260 \, \omega_{pl}^{-1}$  (plain lines) and inverse gyroradii for downstream electrons with energy  $\varepsilon_{\rm NT} \simeq 4k_{\rm B}T_e$  (dashed vertical lines), considering the average *B*-field amplitude in the downstream, for simulations using  $m_i/(m_e Z) = 128$  (blue lines) and 512 (orange lines).

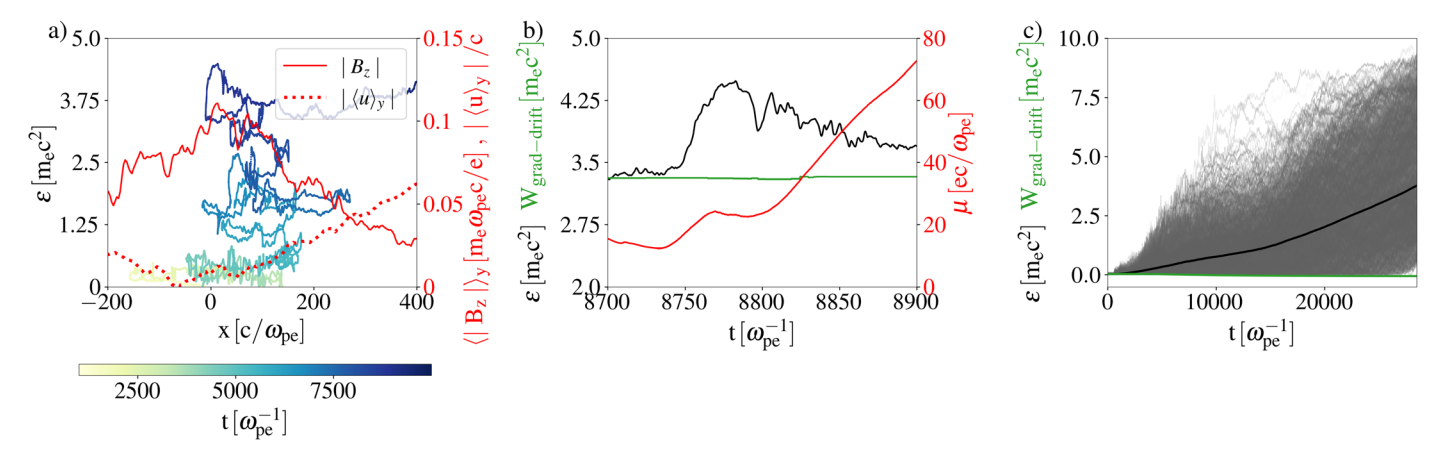


Figure 2. (a) Typical particle energization trajectory as a function of its longitudinal position (i.e., along the *x*-axis) and time (color bar), magnetic field amplitude (red plain line), and flow velocity (red dotted line) averaged along the transverse *y*-direction at  $t \approx 7125 \, \omega_{pe}^{-1}$ . (b) Evolution in time of the electron energy (black line), of the work done by the electric field, assuming the particle motion to be described by the gradient drift approximation (green line), and of the magnetic moment (red line) averaged over the local gyroperiod, during a typical energization event. (c) Evolution of the average particle energy (black line) and the average work within the gradient drift approximation (green line). Shaded gray lines correspond to the energy evolution in time of all particles.

(x = 0). This is consistent with the experimental observations (Figure 1(b)). The separation between the thermal and nonthermal electron populations occurs around  $\varepsilon_{\rm NT} \simeq 4k_{\rm B}T_e$ . We note that at late times electrons reach high enough energy to be injected into DSA, namely the electron gyroradius becomes comparable to inflowing ion gyroradius  $r_{\rm L.e} \simeq r_{\rm L.i}$  in the local magnetic field. In general, this injection condition is given by  $v_e \gamma_e > u \, m_i / (Zm_e)$ . Inspection of the magnetic power spectrum in this region reveals that the initial ion kinetic scale magnetic fields evolve into a broad turbulent spectrum ranging from sub  $c/\omega_{pi}$  scales to  $\sim 10c/\omega_{pi}$ . Most importantly, we observe that the gyroradius of electrons with  $\varepsilon_{\rm NT}$  is close to  $c/\omega_{pi}$  allowing for efficient scattering of these electrons. We have verified this for different values of the ion-to-electron mass ratio, as illustrated in Figure 1(c). This suggests that magnetic turbulence induced by the ion Weibel instability can impact the diffusion of thermal electrons.

To investigate the mechanism responsible for the acceleration of electrons to nonthermal energies we track, in the PIC simulation performed with  $m_i/(Zm_e) = 128$ ,  $\approx 3500$  electrons with high temporal resolution, i.e., equal to the time resolution of the PIC simulation  $\Delta t = 0.285 \ \omega_{pe}^{-1}$ . These electrons have been selected from the nonthermal component at

 $t_{\rm sel} \simeq 2.5 \times 10^3 \, \omega_{pi}^{-1}$ , so as to have even statistics in 15 log-spaced bins with energies  $\varepsilon > 10 \, k_{\rm B} T_e$ .

Electrons are found to gain energy via multiple reflections along the flow direction (i.e., the x-axis), as shown for a typical trajectory in Figure 2(a). This happens while the particle is confined in the shock transition layer, which is the region with strong B-field turbulence, as confirmed by the transversely averaged B-field  $\langle |B_z| \rangle_v$  (red plain line). We also observe (Figure 2(a); red dotted line), that the effective (mean) flow velocity profile in this shock transition, defined as  $\langle u \rangle_{v} = (n_{+}u_{+} + n_{-}u_{-})/(n_{+} + n_{-})$  where the index +(-) refers to the flow moving in the positive (negative) x-direction, is approximately linear. As the shocks move away from each other, we have confirmed that electrons are accelerated by interacting with only one shock front and performing multiple reflections as they are trapped within the shock front, similarly to the case of the particle trajectory illustrated in Figure 2(a) i.e., particles are not gaining energy by interacting with both shocks.

In order to confirm if either SDA or SSDA is responsible for the electron energization, we have computed the magnetic moment of the electrons while they are accelerated  $\mu = m_e \gamma_e^2 v_{e,\perp}^2 / (2 |\mathbf{B}|)$ , where, in the configuration of our 2D3V simulation,  $\perp$  identifies the component in the *xy*-plane

transverse to the  $B_z$  field produced by the Weibel instability and all quantities are averaged over the local gyroperiod of the particle. We observe that  $\mu$  is not conserved. This is illustrated in Figure 2(b), where we focus on one energization event associated with a reflection in the x-direction. This can be understood from the fact that the gyroradius of the electrons is comparable to the scale of the magnetic turbulence produced at the shock. To further confirm this, we have calculated the energy gain experienced by electrons due to the grad-B drift associated with SDA as  $\int E_y \nu_{\nabla B,y} dt$  with  $\nu_{\nabla B} = (-\mu/e) \mathbf{B} \times \nabla B/B^2$ . We can see that both in the case illustrated in Figure 2(b) and for all the selected nonthermal particles (Figure 2(c)) the grad-B drift does not contribute to the nonthermal particle acceleration. We can thus exclude mechanisms such as SDA or SSDA to play a dominant role in this case.

This analysis suggests that in such a high-Mach-number shock the small-scale magnetic turbulence produced at the shock transition is key in controlling particle scattering and the ability of the shock to energize electrons up to injection into DSA. This injection process will be described in the following as a modified-DSA mechanism that occurs while the particles are still confined within the shock front; for thermal electrons, the finite nature of the shock transition must be considered, given that the shock transition is larger than the electron gyroradius, in contrast with the standard DSA.

### 3. Electron Injection via Modified-DSA

The transport and acceleration of electrons in the self-generated turbulence at the shock transition can be described by a Fokker–Planck-type equation (Skilling 1975; Blandford & Eichler 1987; Petrosian 2012). In the diffusive limit, this can be reduced to a diffusion-convection equation for the isotropic part of the distribution  $f_0(x, p)$ , which gives (Reville & Bell 2013)

$$\frac{\partial f_0}{\partial t} + \boldsymbol{u} \cdot \nabla f_0 = \frac{1}{3} \left( \nabla \cdot \boldsymbol{u} - \boldsymbol{u} \cdot \frac{\nabla B}{B} \right) p \frac{\partial f_0}{\partial p} + \nabla \cdot (D \nabla f_0), \tag{1}$$

where D is the spatial diffusion coefficient. As shown in Katou & Amano (2019) and Amano & Hoshino (2022), the component proportional to the gradient of the magnetic field in the energization term (first term on the right-hand side) corresponds to SDA. Since we have shown that this is not the dominant contribution in our configuration, we will focus on the energization term proportional to the gradient of the fluid velocity, which corresponds to first-order Fermi acceleration. From Equation (1) we can then obtain the equation describing standard DSA by assuming that the shock seen by the particles is an infinitely sharp transition, such that  $\nabla \cdot \mathbf{u} = (u_u - u_d)\delta(x)$ , where x = 0 identifies the shock front position, and  $u_u$  and  $u_d$ the upstream and downstream velocities, respectively. For nonrelativistic steady-state shocks  $u_{sh} \ll c$ , considering that electrons are subject to elastic scatterings in the rest frame of the scattering centers, which are moving at  $u_u$  and  $u_d$ , this gives an average energization rate (Bell 1978a, 1978b)

$$\frac{d\varepsilon}{dt}\Big|_{DSA} \simeq \frac{\Delta\varepsilon}{\Delta t}\Big|_{DSA} \simeq \frac{4}{3} \frac{u_u - u_d}{c} \frac{v_e}{c} \frac{\varepsilon}{t_{cont}^{DSA}},\tag{2}$$

where  $\Delta \varepsilon$  is the average energy gain in a cycle around the shock front (i.e., upstream-downstream-upstream) over the time  $\Delta t$  that a particle takes to scatter back and forth across it,  $v_e$  and  $\varepsilon$  are the electron velocity and energy, and  $\Delta t = t_{\rm scatt}^{\rm DSA}$  the scattering time. This is related to the spatial diffusion coefficients in the upstream  $D_u$  and downstream  $D_d$  as

$$t_{\text{scatt}}^{\text{DSA}} = \frac{4D_u}{u_u v_e} + \frac{4D_d}{u_d v_e}.$$
 (3)

The typical acceleration time  $t_{\rm acc}$  defined as  $d\varepsilon/dt\sim\varepsilon/t_{\rm acc}$ , then reads

$$t_{\text{acc}}^{\text{DSA}} = \frac{3}{(u_u - u_d)} \frac{c^2}{v_e^2} \left( \frac{D_u}{u_u} + \frac{D_d}{u_d} \right). \tag{4}$$

This description leads to the well-known power-law energy spectrum with an index dependent only on the shock compression factor (Blandford & Eichler 1987).

For low-energy, near-thermal electron energies, as relevant to the injection process considered here, however, the approximation of an infinitely sharp shock transition cannot be made, as the electron gyroradius is much smaller than the shock transition. Indeed, as we saw in the simulation analysis above, electron energization happens through scattering in the shock transition itself, and thus we must account for the spatial dependence of the different quantities within the shock front. There, the upstream flow slows down and the average flow velocity decreases roughly linearly with the distance from the unperturbed upstream (Figure 2(a) dotted red line). The variation of the flow velocity in the region where the electrons are accelerating modifies the average energy gain  $\Delta \varepsilon$  and consequently the energization rate. Specifically, the difference of the velocities seen at consecutive reflections, that in Equation (2) is a constant equal to  $u_u - u_d$ , has to be replaced by a generic  $\Delta u(\varepsilon)$  that can be a function of the particle energy. Indeed, particles with higher energies can, in principle, explore larger portions of the shock front transition through their diffusive motion and this corresponds to larger values of  $\Delta u$ , as suggested by Figure 2(a) (dotted red line). The extension of the longitudinal electron motion depends on the properties of the diffusion in the self-generated magnetic field turbulence. Given the large amplitude of the magnetic turbulence at the electron gyroradius scales (Figure 2(c)), we consider Bohm diffusion to be a reasonable approximation (we will later verify with the help of PIC simulations) leading to a spatial diffusion coefficient  $D_{\text{Bohm}} = r_{\text{L,e}} v_e / 3$ . Analogously to Equation (3), we expect the scattering time for the modified-DSA to scale as

$$t_{\rm scatt}^{\rm m-DSA} \propto D_{\rm Bohm}/v_e \propto r_{\rm L,e}.$$
 (5)

Within the assumption of Bohm diffusion, the longitudinal diffusive length scales as  $L_{\rm diff} \propto r_{\rm L,e}$ , and consequently  $\Delta u \propto r_{\rm L,e}$ , because of the linear behavior suggested by Figure 2(a). The typical energization rate and acceleration time for the modified-DSA process hence read

$$\frac{d\varepsilon}{dt}\bigg|_{\text{m-DSA}} \simeq \frac{\Delta\varepsilon}{t_{\text{scort}}^{\text{m-DSA}}} \simeq \frac{4}{3} \frac{\Delta u}{c} \frac{v_e}{c} \frac{\varepsilon}{t_{\text{scort}}^{\text{m-DSA}}} \propto \frac{v_e}{c} \varepsilon, \quad (6)$$

$$t_{\rm acc}^{\rm m-DSA} \propto \frac{c^2}{v_e^2} \frac{D_{\rm Bohm}}{\Delta u} \propto \frac{c}{v_e}.$$
 (7)

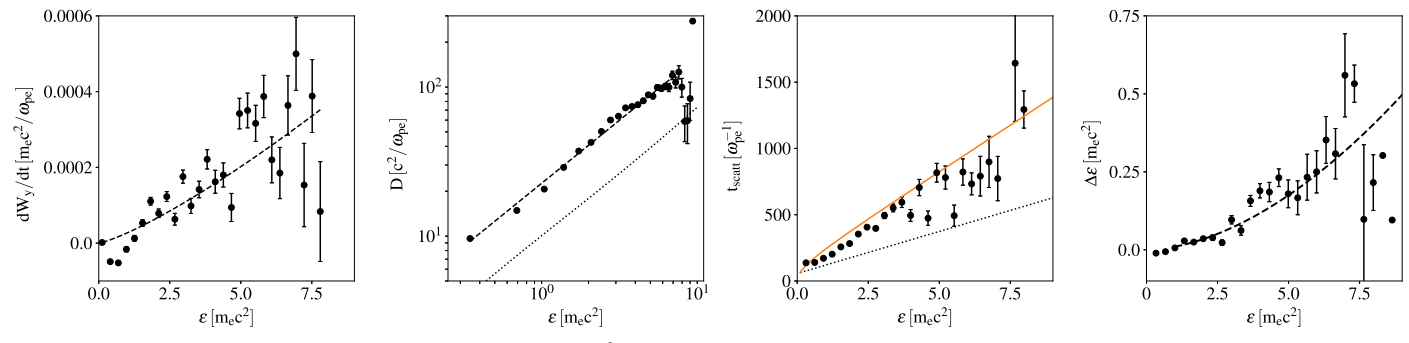


Figure 3. Analysis of the tracked particles for  $t < t_{\rm sel}$  in the region  $\pm 10^3 \ c/\omega_{pe}$ : (a) Average contribution to the energization of  $W_y$  the work of the  $E_y$  component of the electric field. The best fit (dashed line) confirms the linear dependence on the particle energy with  $dW_y/dt \propto \varepsilon^{\alpha}$  with  $\alpha = 1.2 \pm 0.1$ . (b) Spatial diffusion coefficient  $D = \langle \Delta x^2 \rangle/(2\Delta t)$ . The dashed line corresponds to the best fit  $(D \propto \varepsilon^{\beta})$  with  $\beta = 0.85 \pm 0.02$  and the dotted line corresponds to the Bohm diffusion in the average B-field seen by the particles along their trajectories. They both show the same dependence in energy. (c) Averaged scattering time computed as the interval between two consecutive reflections in the particle trajectories time-averaged over the local gyroperiod. Value of half electron gyroperiod (black dotted line) and theoretical prediction (orange line) assuming Bohm diffusion Equation (5). (d) Averaged energy gain due to the work of the  $E_y$  component of the electric field during the reflection events. The fit of  $\Delta \varepsilon \propto \varepsilon^{\delta}$  (dashed line) gives  $\delta = 1.8 \pm 0.2$ .

This suggests that contrary to what is expected for standard DSA, the acceleration time is independent of energy for high energy (relativistic) electrons, and therefore the energization rate increases linearly with the particle energy, up to injection into DSA. Note that in high Mach-number shocks with typical velocity  $\gtrsim 1000~\rm km~s^{-1}$ , the electrons need to be relativistic to reach the threshold for injection. Considering that the shock transition is set by the gyroradius of incoming protons, the condition  $r_{\rm L,e} \simeq r_{\rm L,i}$  entails  $\gamma_e \gtrsim 6$ .

# 4. Validation of Electron Injection Model with PIC Simulations

To test the proposed injection model, the physical quantities that identify the modified-DSA process are extracted from the trajectories of the electrons tracked in the PIC simulation of Section 2. We first analyze the dependence of the energization rate on the electron energy. We have checked that for nonthermal particles their energization is dominated by the perpendicular electric field  $E_{v}$ , while the thermal component is primarily heated by the longitudinal  $E_x$  component. Thus, our theoretical description of the nonthermal particle acceleration accounts for the work  $W_{v}$  of the  $E_{v}$  component of the electric field, which is predominantly produced by the advection of the magnetic field  $B_z$  along the x-direction. The average energization rate  $dW_{\nu}/dt$ , shown in Figure 3(a) is measured considering the trajectories of each tracked particle up to  $t_{\rm sel}$ , in a region of  $\pm 10^3 \, c/\omega_{pe}$  around the midplane, which contains both shock fronts and the shocked downstream at all times  $t < t_{sel}$ . The best fit confirms a near-linear dependence on energy,  $dW_y/dt \propto \varepsilon^{\alpha}$  with  $\alpha \simeq 1.2 \pm 0.1$ , and consequently an acceleration time  $t_{\rm acc}^{\rm m-DSA}$  independent from the particle energy. This is consistent with the scaling predicted in Equation (6), i.e., an energization rate  $\propto v_e \varepsilon \propto \varepsilon^{1.1}$  when considering mildly relativistic particles as appropriate for the simulation.

To further confirm our interpretation of this scaling, we study the dependence on the particle energy of each term on the right side of Equation (6). Since the scattering time is strictly related to the diffusion properties, we extract the spatial diffusion coefficient as  $D = \frac{\langle \Delta x^2 \rangle}{2\Delta t}$  with  $\Delta t \simeq 700~\omega_{pe}^{-1}$  a time interval larger than the

local gyroperiod for all particle energies,  $^{7}$  and  $\Delta x$  the corresponding displacement along the x-direction (Figure 3(b)). From the fit  $D(\varepsilon) \propto \varepsilon^{\beta}$  (dashed line), we obtain  $\beta = 0.85 \pm 0.02$ , which confirms that the diffusion coefficient follows quite accurately the scaling predicted by Bohm diffusion in the mildly relativistic regime (dotted line), which is  $D_{\rm Bohm} \propto r_{\rm L,e} v_e \propto \varepsilon^{0.85}$ . Following Equation (5), we see that the scattering time increases as the accelerating electron gyroradius. We verify this with an independent analysis, in which we identify reflection events in the electron trajectories, averaged over the local gyroperiod, and  $t_{\text{scatt}}^{\text{m-DSA}}$  is computed as the interval between two consecutive reflections. The obtained scattering time compares well with the expected theoretical scaling, Equation (5), as shown in Figure 3(c) (orange line). We also report the reference value of the half gyroperiod in the Bfield seen by the electrons at the reflection (black dotted line), to highlight that we are excluding simple rotations in the averaged field from our analysis.

To conclude the investigation of the energy dependence in Equation (6), we verify that  $\Delta u$ , the velocity difference seen by an electron at consecutive reflections, scales as  $r_{\rm L,e}$ . To do that we considered the same reflection events used to compute  $t_{\rm scatt}^{\rm m-DSA}$  and we extracted  $\Delta \varepsilon$ , considering only the work of the  $E_y$  component of the electric field. The fit of  $\Delta \varepsilon \propto \varepsilon^{\delta}$  (dashed line in Figure 3(d)) gives  $\delta = 1.8 \pm 0.2$ , from which  $\Delta u \propto \varepsilon^{0.7 \pm 0.2}$ . This is in reasonable agreement with the dependence on energy of the electron gyroradius that, in this range of energies, is  $\propto \varepsilon^{0.77}$ . This analysis confirms that particles with higher energy can explore a larger portion of the shock front extension and, therefore, a larger variation of the advection velocity.

We note that in the standard Fermi acceleration picture  $\Delta \varepsilon/\varepsilon \propto (u_u/c)^N$ , where N is the order of the Fermi process. This relation is generally used to distinguish between first-order acceleration in nonrelativistic shocks and second-order acceleration in turbulence (Petrosian 2012). In our configuration, the average flow velocity within the shock front, where the acceleration process takes place, decreases from  $\bar{u}=0.125c$  at early times to  $\bar{u}=0.0025c$  at  $t_{\rm sel}$ . Considering all the reflections happening in this interval of time, one can use the time-averaged

 $<sup>\</sup>overline{\phantom{a}}$  We verified that, for different values of the particle energy, the obtained results are independent of the choice of  $\Delta t$ , provided that it is larger than the gyroperiod.

velocity as  $\Delta \varepsilon/\varepsilon \propto (0.064)^N$ . This value is consistent with a linear fit of the data in Figure 3(d), which gives  $\bar{u}/c = 0.05 \pm 0.01$ , and is much larger than the squared velocity (normalized to c) dependence even for the early times. Hence, this suggests the predominance of a first- over second-order Fermi process operating as the injection mechanism.

Given that, while confined in the shock transition region, electrons experience a velocity jump (or equivalently a density compression) between consecutive reflections that is smaller than the total flow velocity variation across the shock front, the energy spectrum produced by this injection mechanism is expected to have a steeper slope than that associated with standard DSA. Because high-energy particles will experience a larger flow velocity jump, the spectrum shape can also become slightly concave (Ellison et al. 2000; Amato & Blasi 2006). Above the injection energy (i.e., when the gyroradius of the electrons becomes comparable to that of the inflowing upstream ions) the spectrum should then evolve to the standard DSA spectrum.

### 5. Conclusions

We have shown that ion kinetic scale magnetic turbulence produced by the Weibel instability in high-Mach-number shocks can be effective in injecting electrons into a nonthermal population via a first-order Fermi process. Results of kinetic simulations for the conditions of recent NIF simulations confirm the ability of this process to accelerate electrons to  $>100k_{\rm B}T_e$ , consistent with the experimental results. We have proposed that this injection process can be described as a modified-DSA mechanism, where within the shock transition electrons interact with converging magnetic turbulence, undergoing Bohm-like diffusion and accelerating via multiple scatterings in a first-order Fermi process. The obtained scaling laws are consistent with the statistical analysis of the accelerated electrons in the self-consistent kinetic simulations. This modified-DSA mechanism represents a natural extension of conventional DSA and could enable the effective injection of electrons in high-Mach-number astrophysical shocks, such as those associated with young supernova remnants and accretion shocks in galaxy clusters.

## Acknowledgments

This work was supported by the US Department of Energy SLAC contract no. DE-AC02-76SF00515 and Lawrence Livermore National Laboratory contract no. DE-AC52-07NA27344. F.F. acknowledges the support by the US DOE Early Career Research Program under FWP 100331 and the European Research Council (ERC-2021-CoG grant XPACE No. 101045172). A.S. acknowledges the support of NSF through grant PHY-2206607. The authors acknowledge the OSIRIS Consortium, consisting of UCLA and IST (Portugal) for the use of the OSIRIS 4.0 framework and the visXD framework. Simulations were run on Theta (ALCF) through an ALCC award and on Quartz through an LLNL Grand Challenge award.

### **ORCID iDs**

A. Grassi https://orcid.org/0000-0003-3314-7060
H. G. Rinderknecht https://orcid.org/0000-0003-4969-5571
G. F. Swadling https://orcid.org/0000-0001-8370-8837
D. P. Higginson https://orcid.org/0000-0002-7699-3788
H.-S. Park https://orcid.org/0000-0002-8285-8275
A. Spitkovsky https://orcid.org/0000-0001-9179-9054
F. Fiuza https://orcid.org/0000-0002-8502-5535

#### References

```
Amano, T., & Hoshino, M. 2007, ApJ, 661, 190
Amano, T., & Hoshino, M. 2008, ApJ, 690, 244
Amano, T., & Hoshino, M. 2022, ApJ, 927, 132
Amano, T., Katou, T., Kitamura, N., et al. 2020, PhRvL, 124, 065101
Amato, E., & Blasi, P. 2006, MNRAS, 371, 1251
Axford, W. I., Leer, E., & Skadron, G. 1977, in 15th International Cosmic Ray
  Conf., 11, 132
Begelman, M. C., & Kirk, J. G. 1990, ApJ, 353, 66
Bell, A. R. 1978a, MNRAS, 182, 147
Bell, A. R. 1978b, MNRAS, 182, 443
Blandford, R., & Eichler, D. 1987, PhR, 154, 1
Blandford, R. D., & Ostriker, J. P. 1978, ApJL, 221, L29
Blasi, P., & Amato, E. 2012, JCAP, 2012, 010
Bohdan, A., Niemiec, J., Kobzar, O., & Pohl, M. 2017, ApJ, 847, 71
Bohdan, A., Pohl, M., & Niemiec, J. 2020, ApJ, 893, 6
Bohdan, A., Pohl, M., Niemiec, J., et al. 2021, PhRvL, 126, 095101
Diesing, R., & Caprioli, D. 2021, ApJ, 922, 1
Drury, L. O. 1983, RPPh, 46, 973
Ellison, D. C., Berezhko, E. G., & Baring, M. G. 2000, ApJ, 540, 292
Fiuza, F., Swadling, G. F., Grassi, A., et al. 2020, NatPh, 16, 916
Fonseca, R. A., Martins, S. F., Silva, L. O., et al. 2008, PPCF, 50, 124034
Fonseca, R. A., Silva, L. O., Tsung, F. S., et al. 2002, LNCS, 2331, 342
Fried, B. D. 1959, PhFl, 2, 337
Grassi, A., & Fiuza, F. 2021, PhRvR, 3, 023124
Gurevich, A., Pariiskaya, L., & Pitaevskii, L. 1966, JETP, 22, 449
Ha, J., Ryu, D., & Kang, H. 2023, ApJ, 943, 119
Hoshino, M., & Shimada, N. 2002, ApJ, 572, 880
Hudson, P. D., & Kahn, F. D. 1965, MNRAS, 131, 23
Johlander, A., Battarbee, M., Vaivads, A., et al. 2021, ApJ, 914, 82
Kato, T. N., & Takabe, H. 2008, ApJL, 681, L93
Katou, T., & Amano, T. 2019, ApJ, 874, 119
Katsouleas, T., & Dawson, J. M. 1983, PhRvL, 51, 392
Krymskii, G. F. 1977, DoSSR, 234, 1306
Lemoine, M., Gremillet, L., Pelletier, G., et al. 2019, PhRvL, 123, 035101
Levinson, A. 1992, ApJ, 401, 73
Marinak, M. M., Kerbel, G. D., Gentile, N. A., et al. 2001, PhPl, 8, 2275
Matsumoto, Y., Amano, T., & Hoshino, M. 2012, ApJ, 755, 109
Matsumoto, Y., Amano, T., Kato, T. N., & Hoshino, M. 2015, Sci, 347, 974
Matsumoto, Y., Amano, T., Kato, T. N., et al. 2017, PhRvL, 119, 105101
Medvedev, M. V., & Loeb, A. 1999, ApJ, 526, 697
Molnar, S. M., Hearn, N., Haiman, Z., et al. 2009, ApJ, 696, 1640
Petrosian, V. 2012, SSRv, 173, 535
Reville, B., & Bell, A. R. 2013, MNRAS, 430, 2873
Ryutov, D. D., Kugland, N. L., Park, H. S., et al. 2012, PPCF, 54, 105021
Sagdeev, R. Z. 1966, RvPP, 4, 23
Sarris, E. T., & Krimigis, S. M. 1985, ApJ, 298, 676
Skilling, J. 1975, MNRAS, 172, 557
Spitkovsky, A. 2007, ApJL, 673, L39
Swadling, G. F., Bruulsema, C., Fiuza, F., et al. 2020, PhRvL, 124, 215001
Treumann, R. A. 2009, A&ARv, 17, 409
Völk, H. J., Berezhko, E. G., & Ksenofontov, L. T. 2005, A&A, 433, 229
Weibel, E. S. 1959, PhRvL, 2, 83
```